

Observations of submesoscale eddy-driven heat transport at an ice shelf calving front

Drew M. Friedrichs^{1,2}[✉], Jasmin B. T. McInerney^{1,2,3}, Holly J. Oldroyd¹, Won Sang Lee⁴, Sukyoung Yun⁴, Seung-Tae Yoon⁵, Craig L. Stevens^{3,6}, Christopher J. Zappa⁷, Christine F. Dow⁸, Derek Mueller⁹, Oscar Sepúlveda Steiner¹⁰ & Alexander L. Forrest^{1,2}

Antarctica's ice shelves buttress the continent's terrestrial ice, helping slow the loss of grounded ice into the ocean and limiting sea level rise. Ice-ocean interaction plays a critical role in ice shelf stability by driving basal melt rates. Consequently, improved prediction of the future state of ice shelves lies in understanding the coastal ocean mechanics that deliver heat to their cavities. Here, we present autonomous glider-based observations of a coherent structure at the calving front of a cold-water cavity ice shelf (Nansen Ice Shelf, East Antarctica). This ~10 km-wide eddy dominated the local ocean circulation in the austral summer of 2018/2019, promoting an upwelling of cold ice shelf water and a deepening of warm surface water. Microstructure turbulence measurements show a resulting maximum vertical heat transport of 10 W m^{-2} at depths equivalent to the ice shelf draft. Similar eddy-driven heat transport further into the ice shelf cavity would support enhanced summertime melt in regions of shallower ice draft.

¹Department of Civil and Environmental Engineering, University of California, Davis, Davis, CA, USA. ²Tahoe Environmental Research Center, University of California, Davis Incline Village NV, USA. ³National Institute of Water and Atmospheric Research, Wellington, New Zealand. ⁴Korea Polar Research Institute, Incheon, Republic of Korea. ⁵School of Earth System Sciences, Kyungpook National University, Daegu, Republic of Korea. ⁶Department of Physics, University of Auckland, Auckland, New Zealand. ⁷Lamont-Doherty Earth Observatory of Columbia University, Palisades, New York, NY, USA. ⁸Department of Geography and Environmental Management, University of Waterloo, Waterloo, ON, Canada. ⁹Water and Ice Research Laboratory, Department of Geography and Environmental Studies, Carleton University, Ottawa, ON, Canada. ¹⁰Eawag, Swiss Federal Institute of Aquatic Science and Technology, Surface Waters - Research and Management, Kastanienbaum, Switzerland. ✉email: amfriedrichs@ucdavis.edu

The melting of ice shelves occurs via multiple modes, according to the characteristics of the seawater beneath the ice: cold/warm deep water (Mode 1/2), or warm surface water (Mode 3)¹. Localized melt may support the growth of basal channels along the underside of ice shelves², which have been linked to enhanced strain and fracturing within the ice and may lead to calving events³ and the acceleration of terrestrial ice flows⁴. Within cold-water ice shelf cavities (typically dominated by Mode 1), the transport of freezing-temperature ice shelf water (ISW) along the ice-ocean interface may also result in regions of ice accretion, which is expected to level the ice shelf bottom topography⁵. Though warm-cavity ice shelves (dominated by Mode 2 melt) have been the focus of recent literature due to their vulnerability to rapid retreat⁶, Antarctic cold-cavity ice shelves cover more surface area⁷ and several have exhibited high-profile ice shelf fracturing events (e.g., Mertz Glacier Tongue⁸; Nansen Ice Shelf⁹; Voyeykov Ice Shelf¹⁰). It is thus necessary to resolve the forcing mechanisms behind the transport of heat¹¹ and meltwater¹² beneath cold-cavity ice shelves to determine their susceptibility to basal channeling and resulting ice shelf break up.

Most insights into ocean-ice shelf interaction come at the smallest or largest scales, through the pairing of melt rate parameterizations with detailed local observations, or general circulation models with regional surveys, respectively¹³. Intermediate scale circulation phenomena, such as submesoscale eddies (diameter less than 50 km), are known to play a vital role in ocean heat transport¹⁴ but are particularly difficult to quantitatively investigate due to their requirement of maintaining both high resolution and large domains while running simulations or collecting observations. This is especially true along the Antarctic coastline, where the lack of in situ measurements may result in poorly constrained modelling efforts.

On the Antarctic continental shelf, the high latitude and summertime stratification permits intense eddy fields with the potential to play a leading role in heat exchange in the vicinity of ice shelves. A widely published connection between eddies and Antarctic ice melt is through the onshore delivery of warm Circumpolar Deep Water far beneath warm-water ice shelves, promoting Mode 2 melting¹⁵. At cold-water ice shelves, on the other hand, eddy-resolving models have suggested that coastal eddies may transport colder deep water (High Salinity Shelf Water; HSSW)^{16,17} but are more likely to impact melt through the delivery of warm Antarctic Surface Water (ASW) beneath the ice shelf calving front^{11,18}. The formation and behavior of these

eddies are sensitive to ice shelf front conditions, including basal melting and ice shelf front roughness¹⁹, surface buoyancy flux from HSSW formation¹⁶, and sea floor topography¹⁷. Eddy-resolving models are also sensitive to grid size^{16,20} which motivates the common theme of a need for more in situ observations. Near-ice shelf oceanography is frequently measured by a combination of through-ice¹⁸ and open-ocean moorings²¹ supplemented by ship-based profiling²², though each of these methods struggle to match the high resolution (sub-km horizontal spacing) and large spatial coverage (10s of kilometers) necessary for resolving submesoscale features. Autonomous underwater vehicles show promise for investigating near-²³ and sub-ice shelf oceanography²⁴ at these scales, with quieter buoyancy-driven gliders allowing for direct measurements of microstructure turbulence²⁵ via a cost-effective platform²⁶.

To the best of our knowledge, there have not been successful sub-ice shelf glider-based turbulence measurements until now. Here, we present ship- and autonomous underwater glider-based observations of submesoscale eddy-driven heat and water mass transport within Terra Nova Bay (TNB), in front of and beneath the calving front of the Nansen Ice Shelf (NIS; Fig. 1). Velocity and conductivity-temperature-depth (CTD) measurements reveal a submesoscale cyclonic eddy, which increases the depth of the ASW layer while simultaneously upwelling HSSW and ISW. Vertical heat flux derived from microstructure turbulence measurements shows that heat transport is enhanced at depths comparable to the minimum ice shelf thickness. We suggest that similar eddies form throughout the summertime in TNB and may support local variations in ice shelf melt rate, enhancing basal channels and putting the ice shelf at risk to massive calving events.

Results & discussion

Study site. TNB is a latent heat polynya in the western Ross Sea, bounded to the south by the Drygalski Ice Tongue (DIT) and to the west by the NIS (75°S 163°E). Offshore, the bay is greater than 800 m in depth, though it shoals to closer to 600 m near the NIS front and less than 400 m to the north, near Inexpressible Island (Fig. 1b). The NIS is a small (~2000 km²), cold-cavity ice shelf that originates from the Reeves and Priestley glaciers. Its frontal ice draft ranges between 150 and 250 m below the ocean's surface, including a notable basal channel along the glaciers' suture zone³. The ice shelf exhibits extreme katabatic wind events²⁷, which, in

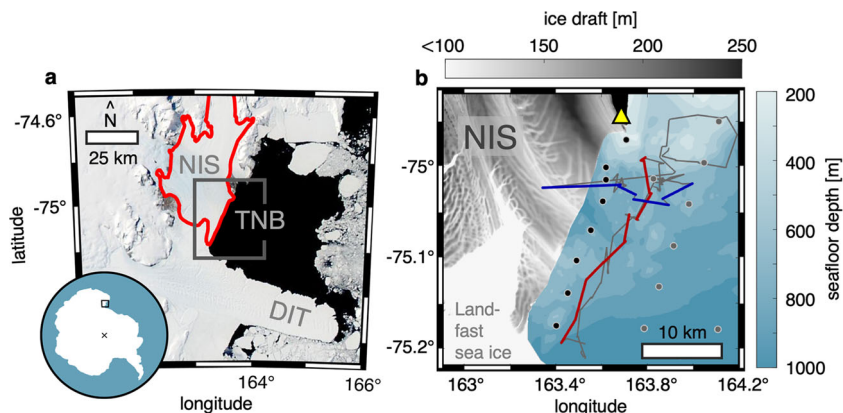


Fig. 1 Site map. **a** MODIS imagery (NASA Worldview) of the study site from 5 January 2019, showing Terra Nova Bay (TNB), the Nansen Ice Shelf (NIS; red outline), and the Drygalski Ice Tongue (DIT). **b** Ice draft, seafloor bathymetry, and collected data. Colored lines indicate glider transects directed approximately parallel to (NE-SW; red) and perpendicular to (E-W; blue) the NIS calving front. Black circles indicate ship CTD/LADCP profiles along a transect parallel to ice shelf front. Grey lines/circles indicate other collected glider/ship data not included in these transects. The yellow triangle indicates the location of Automatic Weather Station Manuela on Inexpressible Island.

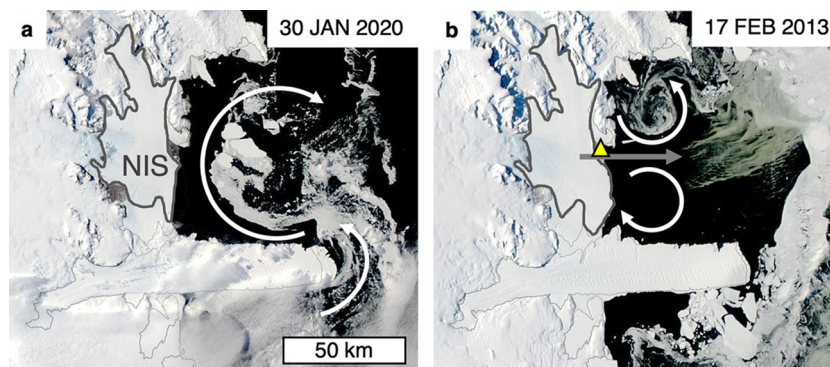


Fig. 2 Terra Nova Bay circulation. MODIS imagery (NASA Worldview) of TNB shows the signature of surface currents (white arrows) in sea ice. a Typical summertime anticyclonic gyre within TNB driven by the deflection of the coastal current around the DIT. **b** Summertime submesoscale eddies produced by strong westerly wind (grey arrow) off the NIS (grey outline) over Inexpressible Island (yellow triangle).

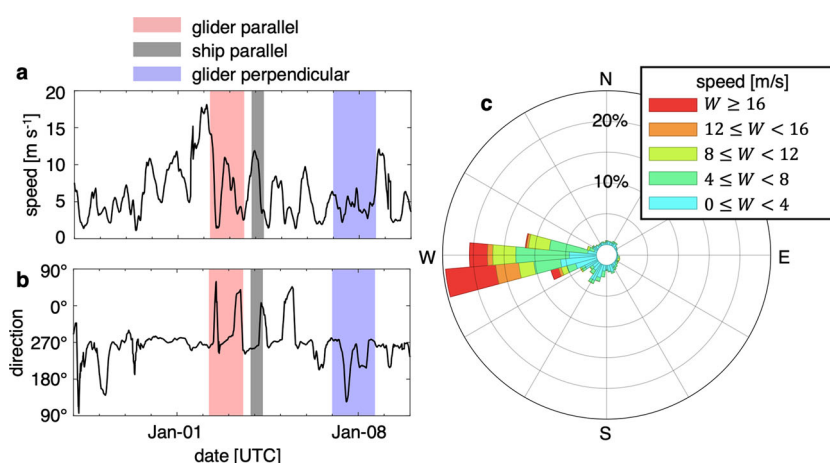


Fig. 3 Atmospheric data from automatic weather station Manuela. a Hourly wind speed, where shaded regions correspond to the time periods over which the data was collected. **b** Hourly wind direction (from). **c** Compass plot of wind speed and direction corresponding to the data in **a**, **b**.

austral winter, promote rapid sea-ice formation in the TNB polynya and the creation of HSSW (potential density anomaly $\theta_\rho > 28 \text{ kg m}^{-3}$). Penetrative convection mixes the bay and HSSW likely spreads to the NIS grounding line²⁸. This spread causes basal melt (Mode 1¹) and the formation of a layer of very cold ISW (potential temperature $\theta_T < -1.94 \text{ }^\circ\text{C}$), which rises above the dense HSSW and may become supercooled while exiting the ice shelf cavity. In summer months, TNB becomes stratified following the formation of a 100 m-thick layer of warm and fresh ASW ($\theta_T > -1.3 \text{ }^\circ\text{C}$), limiting remnant HSSW to depths below 500 m²². There is a northward alongshore current in the region that deflects counter-clockwise around the Drygalski Ice Tongue²⁹ and feeds the basin-scale (40 km-diameter) gyre in the bay²² (Fig. 2a). Summertime stratification sustains smaller, submesoscale eddies in the bay (Fig. 2b and Supplementary Figs. S1 and S2), which have been previously correlated with increased westerly winds through satellite imagery of loose sea ice³⁰ but have not yet been resolved with oceanographic data or circulation models.

Data collection. TNB and the NIS calving front were visited in the austral summer of 2018/19 as part of a research voyage aboard the Research Vessel Ice Breaker ARAON (Korea Polar Research Institute). A Teledyne Slocum G2 glider was deployed from the R/V ARAON between 31 December and 10 January, completing 208 vertical profiles to maximum depths between 100

and 1000 m over approximately 160 km, including a stretch of 18 profiles that reached 6.5 km into the NIS cavity. The glider was equipped with a SeaBird SBE-41 CTD sensor and a Rockland Scientific MicroRider for microstructure temperature measurements. Two glider transects are presented in this paper: a series of dives along headings approximately parallel to (NE-SW; 27 km, 26 profiles) and perpendicular to (E-W; 21 km, 26 profiles) the NIS (Fig. 1b). The timing and location of an additional parallel glider transect (SW-NE) is presented in the Supplementary Information (Supplementary Figs. S3 and S4). Ship-based profiling with a CTD and a concurrent Lowered Acoustic Doppler Current Profiler (LADCP) also occurred before, between, and after the glider deployments, which included a transect of 8 profiles parallel to the ice shelf (Fig. 1b). The relative timing of the collected data is presented in Fig. 3. A strong westerly wind was also observed in the days leading up to the presented transect, with daily maximum sustained speeds of 10–17 m s^{-1} from a constant 270° heading (Fig. 3).

Eddy scales. During the glider surveying, HSSW was measured at unusually shallow depths (above 250 m) in a concentrated region less than 10 km from the ice shelf front (Figs. 4a, 5a, c). These observations were collocated with an anomalously deep ASW layer (Figs. 4b, 5b, d), which extended to depths greater than the minimum draft of the NIS calving front ($\sim 150 \text{ m}$)³. A T-S plot of the CTD data from these glider transects is shown in Fig. 6,

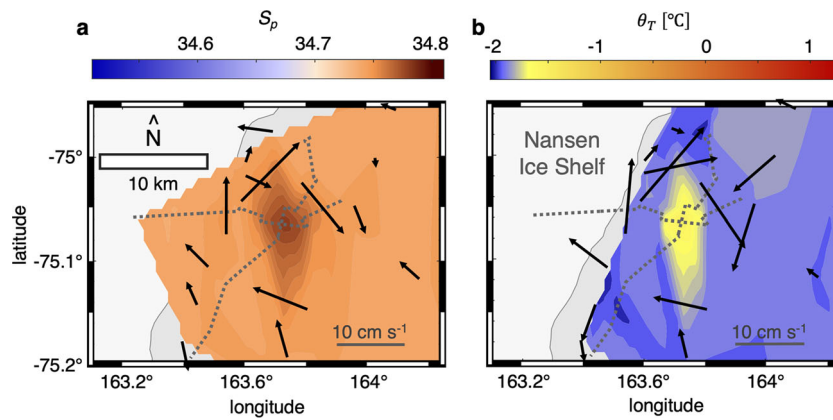


Fig. 4 Eddy horizontal cross sections. **a** Practical salinity and current velocity at 300 m depth. **b** Potential temperature and current velocity at 130 m depth. Light grey polygons show the ice shelf extent. Dashed grey lines indicate glider transects parallel and perpendicular to the NIS calving front, which intersect at the center of the eddy ($r = 0$). The data have been adjusted spatially to offset the northeastward advection of the eddy (see Methods). The grey background signifies regions of no data. Additional maps of surface salinity, surface temperature, salinity at 130 m, and salinity at 300 m are provided in Supplementary Fig. S3.

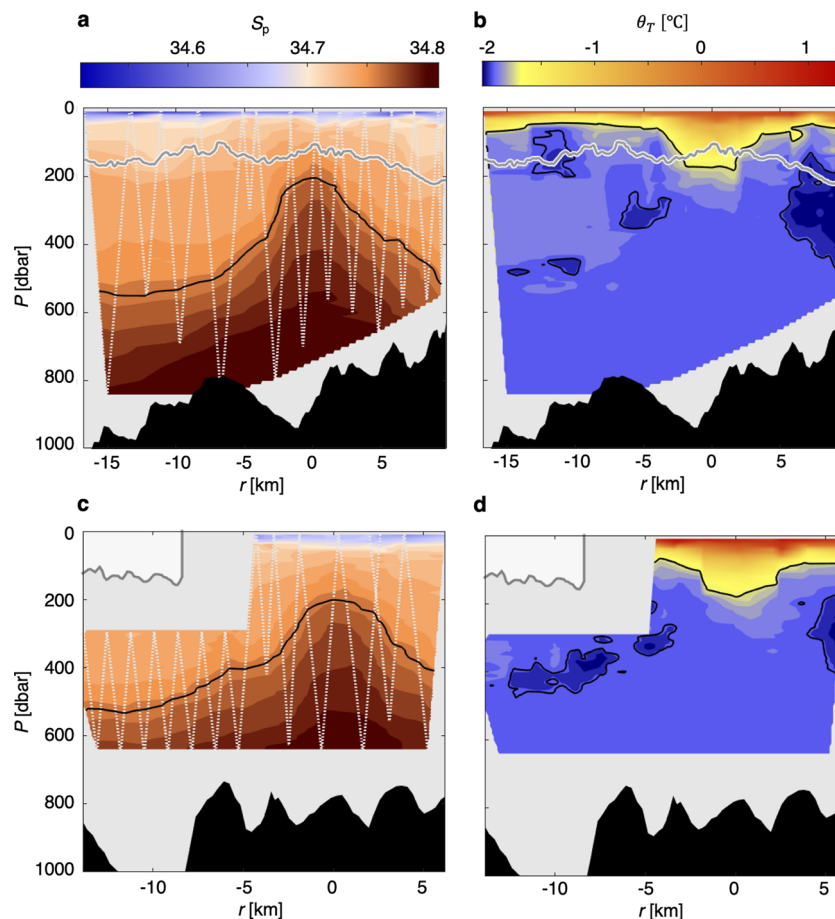


Fig. 5 Eddy vertical cross sections. **a** Practical salinity parallel to the NIS calving front (red lines in Fig. 1b). **b** Potential temperature parallel to the NIS calving front. **c** Practical salinity perpendicular to the NIS calving front (blue lines in Fig. 1b). **d** Potential temperature perpendicular to the NIS calving front. Grey lines in **a**, **b** and light grey polygons in **c**, **d** provide the nearby ice draft. Black contours in **b** and **d** above/below 200 m show the extent of ASW/ISW. Vertical dashed lines show the extent of the data (glider path) before interpolation and black regions indicate seafloor bathymetry. The grey background signifies regions of no data. Vertical cross sections of data observed during eddy formation are provided in Supplementary Fig. S5.

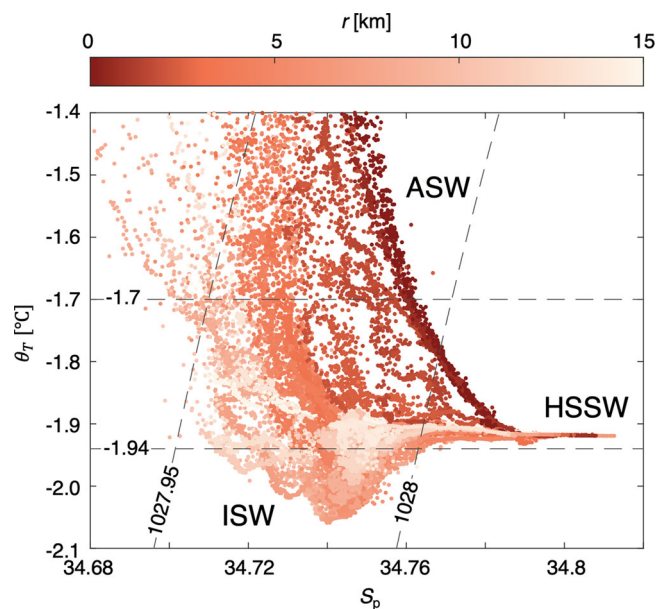


Fig. 6 T-S Plot. Practical salinity versus potential temperature for the glider transects perpendicular to and parallel to the NIS calving front, colored by distance from the center of the eddy. Isotherms define ASW ($>-1.7^{\circ}\text{C}$) and ISW ($<-1.94^{\circ}\text{C}$), while isopycnals define HSSW ($>1028\text{ kg m}^{-3}$).

demonstrating the mixture of ASW and HSSW near the center of this upwelling/downwelling ($r=0$). A layer of ISW was also observed rising in front of the ice shelf (Fig. 5d) to above the maximum NIS draft ($\sim 300\text{ m}$)³ and was notably absent in the center of the feature (from $r=-3$ to 3 km in Fig. 5b, d), likely displaced by the rising HSSW. Seawater velocities collected along the front of the ice shelf indicated a cyclonic (clockwise in the Southern Hemisphere) circulation in the region (Fig. 4), strong enough to account for these anomalous observations. Together, these observations suggest the existence of a subsurface, cyclonic thinny, or an eddy that pulls the main thermocline upward and the seasonal thermocline downward³¹. Insight into similar cyclonic eddies at this scale is limited, although examples of anticyclonic subsurface eddies are linked to localized mixing³² and the storage and transport of intermediate waters far from their source^{19,33}.

The eddy observed in TNB was estimated to be 10 km in diameter and 450 m in height following insight from cross sections of seawater density through the eddy (Fig. 7a, c). The internal Rossby radius of deformation ($R \sim \text{km}$) was smaller than the observed eddy radius, suggesting that rotational effects must be considered. Similarly, the exchange time scale over which the eddy was expected to collapse without Coriolis forcing ($T_c \sim 5\text{ h}$) is much smaller than the 5 days over which it was observed, indicating that the eddy was in a rotational balance³⁴. The eddy was observed to be coupled to the northward coastal current ($\sim 1\text{ cm s}^{-1}$) which suggests that it would eventually travel northward and fall out of geostrophic balance in the shallower water north of Inexpressible Island over several weeks, though satellite imagery of sea ice movement suggests a typically more dynamic environment, with eddy collapse occurring on the order of one week (Supplementary Fig. S1). Eddy azimuthal velocities were estimated from the glider density data through an assumed geostrophic balance (Fig. 7b, d) and agree well with the speeds measured by the LADCP (Fig. 7f), suggesting that the geostrophic component dominates the absolute current velocity. The maximum azimuthal speeds of $\omega = 18\text{ cm s}^{-1}$ were also an order of magnitude larger than the maximum predicted tidal velocities in

the region (see Methods). The LADCP revealed an additional return flow of deep water into the ice shelf cavity beneath the eddy, approximately constrained to the deepest bathymetry (below 700 m ; see Supplementary Fig. S7), indicating that the deepest water was under additional forcing.

Eddy-driven vertical heat transport. Vertical temperature gradients near the NIS are distributed according to the different TNB water masses, with a large temperature gradient in the ASW layer, slightly elevated gradients in the ISW, and nearly isothermal HSSW (Fig. 8a, b). The subsurface eddy restructures the thermocline, which has two major implications for the vertical heat transport in the water column. Firstly, the glider-based microstructure sampling in TNB shows elevated turbulent mixing in the ASW above the eddy core: temperature variance dissipation rate, χ , is larger than $10^{-9}\text{ }^{\circ}\text{C}^2\text{ s}^{-1}$ in front of the ice shelf, down to 150 m depth (at $r=-3$ to $+3\text{ km}$ in Fig. 8c, d). This leads to local regions of elevated heat transfer ($J_h = 10\text{ W m}^{-2}$) away from the warm surface at depths equivalent to the minimum ice thickness (Fig. 8e, f). Secondly, there is also elevated χ of 10^{-10} to $10^{-9}\text{ }^{\circ}\text{C}^2\text{ s}^{-1}$ in the ISW outside the eddy (Fig. 8c, d), which is still an order of magnitude larger than the HSSW background values ($\chi < 10^{-11}\text{ }^{\circ}\text{C}^2\text{ s}^{-1}$). Heat flux is thus directed into the ISW from both above and below. The eddy displaces the ISW upward, which, on the western side of the eddy, draws 10 W m^{-2} downward and away from the calving front of the NIS (at $r=-12$ to -5 km in Fig. 8f). This occurs at depths above 300 m , approaching the maximum thickness of the nearby ice. The result of this analysis is a complex pattern of vertical heat transport at the NIS calving front that is highly dependent on the position and size of the eddy.

Eddy influence on ice shelf melt. Several potential forcing mechanisms exist in TNB that would support the repetitive formation of such an eddy, including persistent katabatic winds off the ice shelf³⁰, the deflection of the northbound coastal current around the DIT²⁹, and horizontal pressure gradients from distributed ISW outflow (Dow et al., 2022, in preparation). As these are each persistent features of TNB, the eddy observed in this study is expected to be a recurring feature of the southwest corner of the bay, coupled with a clockwise, anticyclonic eddy in the northwest. Satellite images occasionally show the surface expression of submesoscale eddies forming in response to westerly winds through the movement of sea ice³⁰ (Fig. 2b and S2), but the TNB Polynya is sea ice-free throughout much of the year. This is particularly true in the southwest corner of TNB as it is strongly sheltered by the DIT from sea ice carried by the northward coastal current. Lack of evidence in sea ice distribution should not preclude the existence of eddies, however, as the formation of sea ice likely indicates poor conditions for eddy formation; the rapid HSSW formation that accompanies sea ice production in TNB results in convection that may destroy the density gradients necessary to sustain these eddies. With rapid sea ice production in the wintertime, this eddy is expected to be a summertime phenomenon.

In its observed position, the submesoscale eddy from January 2019 is likely too far from the NIS cavity for the discussed vertical heat fluxes to considerably influence ice shelf melt rate, especially regarding the deepened ASW layer several kilometers offshore (Fig. 9a). Recent mesoscale eddy-resolving models of larger cold cavity ice shelves, however, support the idea that other iterations of the TNB eddy may protrude further into the NIS cavity. Eddies enter the Ronne Ice Shelf cavity, for example, due to the intersection of a Weddell Sea rim current with the ice shelf¹⁶, a situation reminiscent of the westward current just north of the

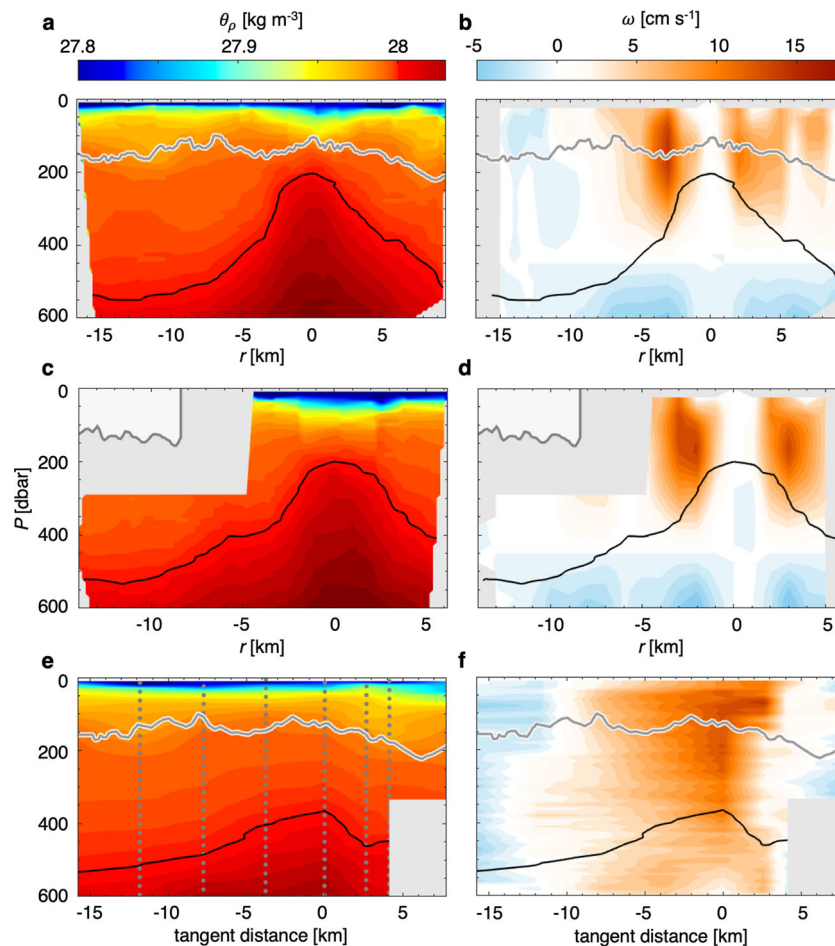


Fig. 7 Eddy azimuthal velocities. **a** Potential density from glider measurements parallel to the NIS calving front (red lines in Fig. 1b). **b** Estimated eddy azimuthal velocity (positive clockwise/cyclonic) from the glider data in **a**. **c** Potential density from glider measurements perpendicular to the NIS calving front (blue lines in Fig. 1b). **d** Estimated eddy azimuthal velocity (positive clockwise/cyclonic) from the glider data in **c**. **e** Potential density from the ship CTD transect parallel to the NIS calving front (tangent to, not bisecting the eddy). **f** Measured eddy azimuthal velocity from the ship LADCP, concurrent with the ship CTD in **e**. LADCP current velocities in Earth-normal components are provided in Fig. S7. Grey lines in **a**, **b**, **e**, and **f** and light grey polygons in **c** and **d** provide the nearby ice draft. Vertical dashed lines in **e** show the extent of the data (ship CTDs) before interpolation. Black contours show the upper extent of the HSSW. The grey background signifies regions of no data.

DIT (Fig. 2a). Other simulations suggest that mesoscale eddies are also able to intrude beneath the Ross Ice Shelf, crossing the potential vorticity gradients that exist at the ice shelf front²⁰. A meltwater wedge has been suggested as a mechanism in which melt from the vertical ice shelf face alters near-ice isopycnals and may allow these eddies to guide warm surface water into a cold-water ice shelf cavity¹¹. Finally, enhanced ice front melt rates derived from satellite altimetry measurement over the NIS (Dow et al. 2022, in preparation) support the occurrence of Mode 3 melt at the ice shelf front and within the NIS basal channel.

An eddy extending beneath the NIS would 1) allow heat to access the thinnest regions of the ice shelf and 2) force the upwelling of ISW beneath the ice, lowering melt rates in regions of deeper ice draft (Fig. 9b). The existing basal channel beneath the NIS makes the ice shelf particularly vulnerable to these phenomena. Although the channel was likely formed upstream by the coalescence of two glaciers, the combination of warm surface water inflow into the basal channel and limited melt on the bordering basal ridges would exacerbate the region of minimal ice shelf thickness previously linked to ice shelf fracturing³.

Implications. There has been a recent push to identify the melt rates and calving frequency at each of the ice shelves surrounding

Antarctica^{7,35,36} and it is likely that eddying behavior similar to our observations exists offshore of many of these ice shelf systems. The East Antarctica coastline hosts several wind-forced (or latent heat) polynyas comparable to TNB that also exhibit complex interaction between alongshore current and coastal cape or ice shelf promontories³⁷. Several of these ice shelf systems present a higher risk of dramatic retreat when compared to the NIS by exhibiting higher melt rates (e.g., Dibble, Vincennes) or a much more active calving front (e.g., Ninnis, Holmes)⁷. Few studies outside TNB, however, have considered that coastal eddies may deliver warm water beneath ice shelves to drive localized melt and trigger fracturing. Existing summertime hydrographic measurements along East Antarctic ice shelves should be investigated for the signatures of cyclonic meso- and submesoscale eddies, such as the interaction of unusually deep ASW with unusually shallow HSSW (Fig. 6) or satellite-based imagery of rotational features³⁰. Anticyclonic mode water eddies³¹, though not examined here, should also be noted due to their ability to transport water at intermediate depths far from its source³³. The localized ISW outflow seen at the NIS (Dow et al. 2022, in preparation) is a candidate for transport by anticyclonic eddies.

Few studies observe coastal Southern Ocean mechanics at the scales necessary for resolving submesoscale eddies. These eddies

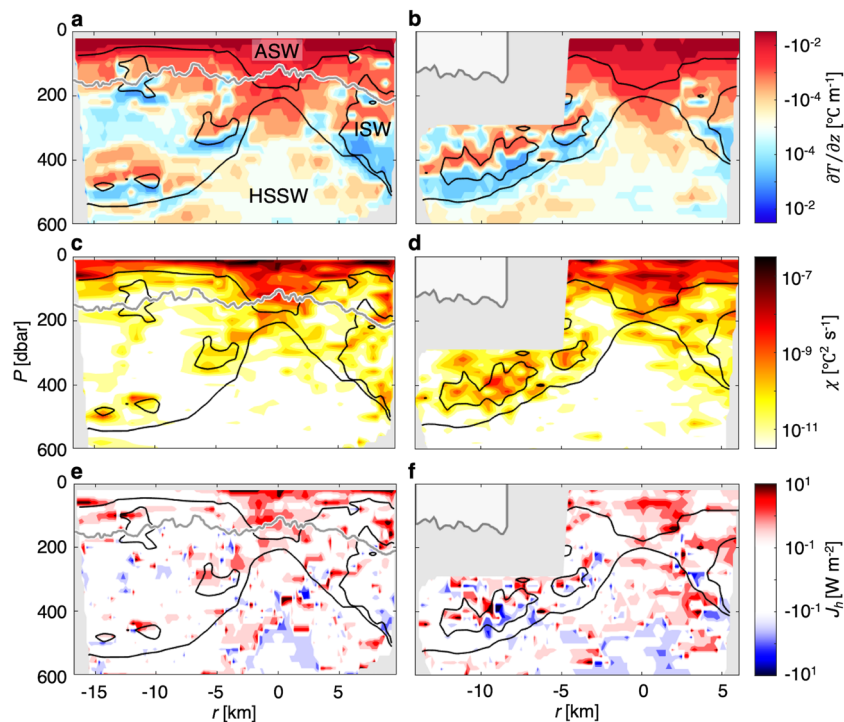


Fig. 8 Eddy heat transport. **a, b** Vertical temperature gradient, where negative values (red) indicate decreasing temperature with increasing depth. **c, d** Rate of temperature variance dissipation. **e, f** Vertical heat flux, where red indicates downward heat transfer. **a, c, and e** are interpolated from the glider transect parallel to the NIS calving front (red lines in Fig. 1b), where grey lines indicate the nearby ice draft. **b, d, and f** are interpolated from the glider transect perpendicular to the NIS calving front (blue lines in Fig. 1b), where light grey polygons show the nearby ice draft. Black lines show the extent of ASW, ISW, and HSSW (defined in Figs. 4 and 5) and the grey background signifies regions of no data. Similar diagrams of heat transport during eddy formation are provided in Supplementary Fig. S6.

require sub-km scale resolution in both models and observational strategies, which may be why evidence of their existence is rare. To further elucidate the role of submesoscale eddies in ice shelf cavity-ocean exchange, the design of adequate field surveys resolving these intermediate scales is essential. Insight into the behavior of submesoscale eddies in TNB would benefit from sub-ice shelf measurements to confirm that ASW is observed within the basal channel. The remote sensing of sea surface features (temperature, elevation, and sea ice motion) shows promise for identifying mesoscale eddies in open water polynyas, but large scale (10–100 km) autonomous underwater vehicle surveys are likely required for spatially distributed observations beneath ice. Circulation modelling efforts must also ensure a submesoscale-resolvent grid size to accurately predict the sensitivity of eddies to changes in Antarctic coastal circulation, such as increased ice shelf water outflow from beneath the NIS or altered DIT geometry.

In this paper, evidence is presented for the eddy-driven restructuring of water masses near cold-cavity ice shelves, as both warm ASW and cold ISW are introduced to depths where interaction with the ice shelf calving front is possible. A mechanism is then suggested for the amplification of basal channels via concentrated melt, which has the potential to increase the frequency of large calving events³ and the acceleration of terrestrial ice flows⁴. It is therefore critical that ice cavity observations and models accurately resolve submesoscale eddies to provide more complete insight into ice-front heat transport regimes.

Methods

External data products. Satellite imagery of the site (Fig. 1a) is from the NASA Worldview application, part of the NASA Earth Observing System Data and

Information System. Ice shelf draft (Fig. 1b) was derived via hydrostatic inversions of the Reference Elevation Model of Antarctica³⁸. Wind data were recorded by Automatic Weather Station Manuela (Inexpressible Island; 74.946°S, 163.687°E), part of the University of Wisconsin-Madison Automatic Weather Station Program. Visualization of the wind data (Fig. 3c) was made possible by the Wind Rose MATLAB function³⁹. Tidal data were provided by the Circum-Antarctica Tidal Simulation model⁴⁰; the mean tidal current during the surveying (31 December to 9 January) was 0.7 cm s^{-1} .

Oceanography and eddy calculations. Sea floor bathymetry was produced by multi-beam sonar aboard the research cruise (Fig. 1b). Derived oceanographic properties (salinity, density, etc.) were calculated with the Gibbs Seawater Oceanographic Toolbox⁴¹. The practical salinity from the glider was corrected by a constant -0.015 using historic measurements of TNB salinity and concurrent ship-based CTD profiling. The eddy Rossby radius R was calculated following

$$R = c/f \quad (1)$$

where $f \approx -1.4 \cdot 10^{-4} \text{ s}^{-1}$ is the Coriolis frequency at -75° latitude and

$$c = (g' \cdot h)^{1/2} \quad (2)$$

is the internal wave speed, with

$$g' = g \cdot \Delta\rho/\rho_0 \quad (3)$$

as reduced gravity, $\Delta\rho = -0.03 \text{ kg m}^{-3}$ as the difference in density from the interior to the exterior of the eddy, $\rho_0 = 1030 \text{ kg m}^{-3}$ as a reference density, and $h = 225 \text{ m}$ as half of the eddy height. The eddy time scale for exchange T_e was calculated following

$$T_e = r/c \quad (4)$$

where the eddy radius $r \approx 5 \text{ km}$ was determined from the horizontal density gradient observed across the eddy (Fig. 7) and c defined according to Eq. 2. The fully formed eddy was first observed during the second glider transect (NE-SW) at 06:00 on 2 January and was last observed during the third glider transect (E-W) at 12:00 on January 7, indicating that the eddy existed for at least 5 days. During this time, the eddy traveled to the northwest at an average of 1.1 cm s^{-1} . The time and position of the data in Fig. 4 were adjusted according to this vector to best represent accurate dimensions of the eddy. Eddy azimuthal velocities ω (Fig. 7b, d) were

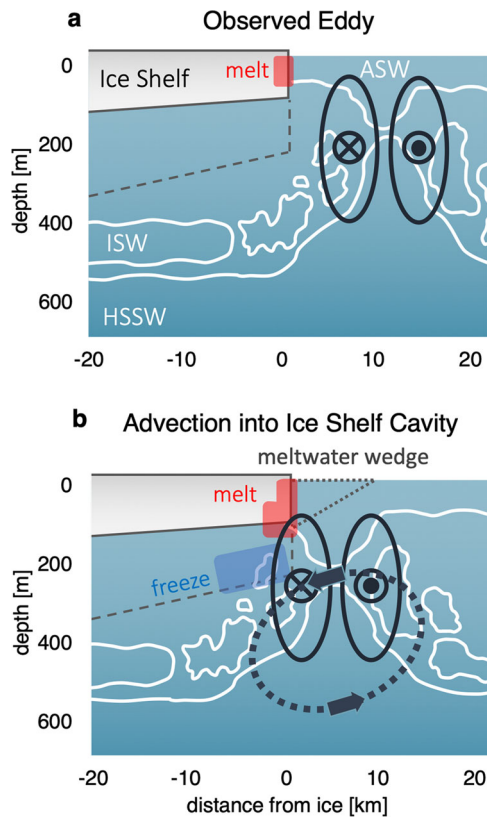


Fig. 9 Eddy schematic. **a** The observed eddy just offshore of the NIS, resulting in minimal heat exchange with the ice base. **b** A hypothesized case of shoreward advection of the observed eddy due to external forcing (arrows), resulting in localized regions of enhanced melt (red) and refreezing (blue) on the underside of the ice shelf. The grey polygon represents the minimum ice shelf thickness within the NIS basal channel, while dashed grey lines show the maximum ice shelf thickness outside of the channel. Tall ovals indicate the extent of the eddy, where \times and \circ indicate motion into and out of the page, respectively. White lines indicate the locations of water masses supported by observations from this survey.

estimated from glider-based CTD data by balancing the observed pressure field against the Coriolis forcing using a geostrophic balance,

$$f \cdot \omega = (1/\rho_0) \cdot (\partial p / \partial r) \quad (5)$$

where p is pressure, under the assumption that there was no horizontal pressure gradient at the bottom of the eddy (450 m; Supplementary Fig. S6c). CTD data from the R/V *ARAON* were processed following the standard procedure recommended by Sea-Bird Electronics⁴². The LADCP profiles were obtained in 5 m bins and were processed using the velocity inversion method⁴³.

Microstructure turbulence. Only data from a single FP07 thermistor of the glider's Rockland Scientific MicroRider were used in this analysis as the second exhibited excessive electronic noise. We confirmed the microstructure temperature recorded by the working probe through comparison with concurrent microstructure shear (also from the MicroRider) and expected values from previous datasets²⁹. Under the assumption of isotropic turbulence, the rate of dissipation of temperature variance²⁵ can be calculated as

$$\chi = 6\kappa \left\langle \left(\partial T' / \partial x \right)^2 \right\rangle \quad (6)$$

where κ is molecular thermal diffusivity and $\partial T' / \partial x$ is the temperature gradient variance measured by the MicroRider as the glider travels in the x -direction. In practice, this calculation involves processing the wavenumber spectrum of the gradient signal. We followed the standard methods⁴⁴ to calculate χ (Fig. 8c, d), which is related to the diffusivity of heat as⁴⁵

$$K_h = 0.5\chi(T_z)^{-2} \quad (7)$$

where T_z is the local vertical temperature gradient (Fig. 8a, b), finally leading to

vertical heat flux,

$$J_h = -\rho c_p K_h T_z \quad (8)$$

(Figure 8e, f), where c_p is specific heat capacity, derived via the MIT Seawater Thermophysical Properties MATLAB Library^{46,47}.

Data availability

The raw MicroRider turbulence data files, as well as the processed CTD, ADCP, and turbulence data that support the findings of this study are available from the Dryad Digital Repository (DOI: 10.25338/B88H1H). Satellite imagery can be accessed from the NASA Worldview application (worldview.earthdata.nasa.gov) and wind data from Automatic Weather Station Manuela can be accessed from the Antarctic Meteorological Research Center (amrc.ssec.wisc.edu).

Code availability

The data processing completed for this paper, including the generation of temperature variance dissipation rate χ , was completed in MATLAB. The custom code necessary for replicating these results is available from the corresponding author upon reasonable request.

Received: 28 September 2021; Accepted: 16 May 2022;

Published online: 22 June 2022

References

- Jacobs, S. S., Helmer, H. H., Doake, C. S. M., Jenkins, A. & Frolich, R. M. Melting of ice shelves and the mass balance of Antarctica. *J. Glaciol.* **38**, 375–387 (1992).
- Alley, K. E., Scambos, T. A., Siegfried, M. R. & Fricker, A. H. Impacts of warm water on Antarctic ice shelf stability through basal channel formation. *Nat. Geosci.* **9**, 290–293 (2016).
- Dow, C. F. et al. Basal channels drive active surface hydrology and transverse ice shelf fracture. *Sci. Adv.* **4**, eaao7212 (2018).
- Reese, R., Gudmundsson, G. H., Levermann, A. & Winkelmann, R. The far reach of ice-shelf thinning in Antarctica. *Nat. Climate Change* **8**, 53–57 (2018).
- Craven, M., Allison, I., Fricker, H. A. & Warner, R. Properties of a marine layer under the Amery Ice Shelf, East Antarctica. *J. Glaciol.* **55**, 717–728 (2009).
- Jenkins, A. et al. West Antarctic Ice Sheet retreat in the Amundsen Sea driven by decadal oceanic variability. *Nat. Geosci.* **11**, 733–738 (2018).
- Rignot, E., Jacobs, S., Mouginot, J. & Scheuchl, B. Ice-shelf melting around Antarctica. *Science* **341**, 266–270 (2013).
- Tamura, T., Williams, G. D. & Ohsima, K. I. Potential regime shift in decreased sea ice production after the Mertz Glacier calving. *Nat. Commun.* **3**, 1–6 (2012).
- Dziak, R. P. et al. Hydroacoustic, meteorologic and seismic observations of the 2016 Nansen ice shelf calving event and iceberg formation. *Front. Earth Sci.* **7**, 183 (2019).
- Arthur, J. F. et al. The triggers of the disaggregation of Voyeykov Ice Shelf (2007), Wilkes Land, East Antarctica, and its subsequent evolution. *J. Glaciol.* **67**, 933–951 (2021).
- Malyarenko, A., Robinson, N. J., Williams, M. J. M. & Langhorne, P. J. A wedge mechanism for summer surface water inflow into the Ross Ice Shelf cavity. *J. Geophys. Res. Oceans* **124**, 1196–1214 (2019).
- Naveira Garabato, A. C. et al. Vigorous lateral export of the meltwater outflow from beneath an Antarctic ice shelf. *Nature* **542**, 219–222 (2017).
- Dinniman, M. S. et al. Modeling ice shelf/ocean interaction in Antarctica: A review. *Oceanography* **29**, 144–153 (2016).
- Su, Z., Wang, J., Klein, P., Thompson, A. F. & Menemenlis, D. Ocean submesoscales as a key component of the global heat budget. *Nat. Commun.* **9**, 1–8 (2018).
- Couto, N., Martinson, D. G., Kohut, J. & Schofield, O. Distribution of Upper Circumpolar Deep Water on the warming continental shelf of the West Antarctic Peninsula. *J. Geophys. Res. Oceans* **122**, 5306–5315 (2017).
- Årthun, M., Holland, P. R., Nicholls, K. W. & Fetham, D. L. Eddy-driven exchange between the open ocean and a sub-ice shelf cavity. *J. Phys. Oceanogr.* **43**, 2372–2387 (2013).
- Hatterman, T., Smedsrud, L. H., Nøst, O. A., Lilly, J. M. & Galton-Fenzi, B. K. Eddy-resolving simulations of the Fimbul Ice Shelf cavity circulation: Basal melting and exchange with open ocean. *Ocean Model.* **82**, 28–44 (2014).

18. Arzeno, I. B. et al. Ocean variability contributing to basal melt rate near the ice front of Ross Ice Shelf, Antarctica. *J. Geophys. Res. Oceans* **119**, 4214–4233 (2014).
19. Li, Y., McGillicuddy, D. J. Jr, Dinniman, M. S. & Klinck, J. M. Processes influencing formation of low-salinity high-biomass lenses near the edge of the Ross Ice Shelf. *J. Marine Sys* **166**, 108–119 (2017).
20. Mack, S. L., Dinniman, M. S., Klinck, J. M., McGillicuddy, D. J. Jr & Padman, L. Modeling ocean eddies on Antarctica's cold water continental shelves and their effects on ice shelf basal melting. *J. Geophys. Res. Oceans* **124**, 5067–5084 (2019).
21. Darelius, E., Fer, I. & Nicholls, K. W. Observed vulnerability of Filchner-Ronne Ice Shelf to wind-driven inflow of warm deep water. *Nat. Commun.* **7**, 1–7 (2016).
22. Yoon, S. T. et al. Variability in high-salinity shelf water production in the Terra Nova Bay polynya, Antarctica. *Ocean Sci.* **16**, 373–388 (2020).
23. Miles, T. et al. Glider observations of the Dotson Ice Shelf outflow. *Deep Sea Res. Part II* **123**, 16–29 (2016).
24. Kimura, S. et al. Ocean mixing beneath Pine Island Glacier ice shelf, West Antarctica. *J. Geophys. Res. Oceans* **121**, 8496–8510 (2016).
25. Peterson, A. K. & Fer, I. Dissipation measurements using temperature microstructure from an underwater glider. *Meth. Oceanog.* **10**, 44–69 (2014).
26. Schofield, O. et al. Slocum Gliders: Robust and ready. *J. Field Robot.* **24**, 473–485 (2007).
27. Bromwich, D. H. & Kurtz, D. D. Katabatic wind forcing of the Terra Nova Bay polynya. *J. Geophys. Res. Oceans* **89**, 3561–3572 (1984).
28. Rusciano, E., Budillon, G., Fusco, G. & Spezie, G. Evidence of atmosphere-sea ice-ocean coupling in the Terra Nova Bay polynya (Ross Sea-Antarctica). *Continent. Shelf Res.* **61**, 112–124 (2013).
29. Stevens, C. et al. The influence of the Drygalski Ice Tongue on the local ocean. *Annal. Glaciol.* **58**, 51–59 (2017).
30. Moctezuma-Flores, M., Parmiggiani, F., Fragiaco, C. & Guierri, L. Synthetic aperture radar analysis of floating ice at Terra Nova Bay—an application to ice eddy parameter extraction. *J. Applied Remote Sensing* **11**, 026041 (2017).
31. McGillicuddy, D. J. Formation of intrathermocline lenses by eddy-wind interaction. *J. Phys. Oceanog.* **45**, 606–612 (2015).
32. Fernández-Castro, B., Evans, D. G., Frajka-Williams, E., Vic, C. & Naveira-Garabato, A. C. Breaking of internal waves and turbulent dissipation in an anticyclonic mode water eddy. *J. Phys. Oceanog.* **50**, 1893–1914 (2020).
33. Xu, L. et al. Observing mesoscale eddy effects on mode-water subduction and transport in the North Pacific. *Nat. Commun.* **7**, 1–9 (2016).
34. Forrest, A. L., Laval, B. E., Pieters, R. & Lim, D. S. S. A cyclonic gyre in an ice-covered lake. *Limn. Oceanog.* **58**, 363–375 (2013).
35. Pritchard, H. et al. Antarctic ice-sheet loss driven by basal melting of ice shelves. *Nature* **484**, 502–505 (2012).
36. Schodlok, M. P., Menemenlis, D. & Rignot, E. Ice shelf basal melt rates around Antarctica from simulations and observations. *J. Geophys. Res. Oceans* **121**, 1085–1109 (2016).
37. Tamura, T., Oshima, K. I., & Hihashi, S. Mapping of sea ice production for Antarctic coastal polynyas. *Geophys. Res. Lett.* **35**, L07606 (2008).
38. Howat, I. M., Porter, C., Smith, B. E., No, M.-J. & Morin, P. The reference Elevation Model of Antarctica. *The Cryosphere* **13**, 665–674 (2019).
39. Pereira, D. Wind Rose. *MATLAB Central File Exchange* (www.mathworks.com/matlabcentral/fileexchange/47248-wind-rose). Retrieved 21 May 2021.
40. Padman, L., Fricker, H. A., Coleman, R., Howard, S. & Erofeeva, L. A new tide model for the Antarctic ice shelves and seas. *Annal. Glaciol.* **34**, 247–254 (2002).
41. IOC, SCOR, and IPSO. The international thermodynamic equation of seawater – 2010: Calculation and use of thermodynamic properties. *Intergovern. Oceanog. Commission, Manuals Guides* **56**, 1–196 (2010).
42. Sea-Bird Scientific. *Seasoft V2: SBE Data Processing* (Sea-Bird Scientific, Bellevue, Washington, 2017).
43. Thurnherr, A. M. *How to process LADCP Data With the LDEO Software* (Columbia University, Palisades, New York, 2014).
44. Piccolroaz, S., Fernández-Castro, B., Toffolon, M. & Dijkstra, H. A. A multi-site, year-round turbulence microstructure atlas for the deep perialpine Lake Garda. *Scientific Data* **8**, 1–20 (2021).
45. Osborn, T. R. & Cox, C. S. Oceanic fine structure. *Geophys. Fluid Dyn.* **3**, 321–345 (1972).
46. Nayar, K. G., Sharqawy, M. H., Banchik, L. D. & Lienhard V, J. H. Thermophysical properties of seawater: A review and new correlations that include pressure dependence. *Desalination* **390**, 1–24 (2016).
47. Sharqawy, M. H., Lienhard V, J. H. & Zubair, S. M. Thermophysical properties of seawater: A review of existing correlations and data. *Desalination Water Treatment* **16**, 354–380 (2010).

Acknowledgements

We thank glider pilot Cordielyn Goodrich and field technician Sébastien Lavanchy, as well as the entirety of the R/V ARAON crew for successful data collection and a safe research voyage. We would also like to credit Rockland Scientific Inc and Teledyne Webb Research for their support throughout the planning and execution of our glider deployments. This study was sponsored by a research grant from the Korean Ministry of Oceans and Fisheries (KIMST20190361; PM22020). C.S. was supported by the NZ Antarctic Science Platform ANTA1801. We acknowledge the use of imagery from the NASA Worldview application (<https://worldview.earthdata.nasa.gov/>), part of the NASA Earth Observing System Data and Information System (EOSDIS). The authors also appreciate the support of the University of Wisconsin-Madison Automatic Weather Station Program for the wind data set, data display, and information, NSF grant number 1924730. Finally, ice shelf DEMs were provided by the Byrd Polar and Climate Research Center and the Polar Geospatial Center under NSF-OPP awards 1543501, 1810976, 1542736, 1559691, 1043681, 1541332, 0753663, 1548562, 1238993 and NASA award NNX10AN61G, with computer time provided through a Blue Waters Innovation Initiative and DEMs produced using data from Maxar.

Author contributions

D.M.F., J.B.T.M., S.Y., and S.T.Y. led the data collection. D.M.F. led the data processing, with contributions from J.B.M. (glider CTD), S.T.Y. (ship CTD and LADCP), C.F.D. and D.M. (ice shelf draft), and O.S.S. (microstructure turbulence). All authors (including H.J.O., W.S.L., C.L.S., C.J.Z., and A.L.F.) assisted in data analysis and manuscript drafting.

Competing interests

The authors declare no competing interests.

Additional information

Supplementary information The online version contains supplementary material available at <https://doi.org/10.1038/s43247-022-00460-3>.

Correspondence and requests for materials should be addressed to Drew M. Friedrichs.

Peer review information *Communications Earth & Environment* thanks Kazuya Kusahara and the other, anonymous, reviewer(s) for their contribution to the peer review of this work. Primary Handling Editors Shin Sugiyama, Heike Langenberg. Peer reviewer reports are available.

Reprints and permission information is available at <http://www.nature.com/reprints>

Publisher's note Springer Nature remains neutral with regard to jurisdictional claims in published maps and institutional affiliations.

 **Open Access** This article is licensed under a Creative Commons Attribution 4.0 International License, which permits use, sharing, adaptation, distribution and reproduction in any medium or format, as long as you give appropriate credit to the original author(s) and the source, provide a link to the Creative Commons license, and indicate if changes were made. The images or other third party material in this article are included in the article's Creative Commons license, unless indicated otherwise in a credit line to the material. If material is not included in the article's Creative Commons license and your intended use is not permitted by statutory regulation or exceeds the permitted use, you will need to obtain permission directly from the copyright holder. To view a copy of this license, visit <http://creativecommons.org/licenses/by/4.0/>.

© The Author(s) 2022